

# Computation of crack tip elastic stress intensity factor in mode I by in-plane electronic speckle pattern interferometry

J. Parra-Michel, A. Martínez, and J.A. Rayas

*Centro de Investigaciones en Óptica A.C.,*

*Lomas del Bosque 115, Col Lomas del Campestre León Guanajuato, México,*

*email: jrpmichel@cio.mx*

Recibido el 15 de abril de 2010; aceptado el 9 de octubre de 2010

In this work, a dual illumination beam system is used to obtain the stress intensity factor in modes one (mode  $I$ ) to mechanical elements during tension testing. The displacement field is obtained by means of electronic speckle pattern interferometry and phase stepping technique. Deformations are calculated by the Stokes differentiation method. Results are compared with a numerical simulation using a finite element analysis technique.

**Keywords:** Stress intensity factor; ESPI; Stokes method; phase stepping.

En este trabajo un sistema de iluminación dual es utilizado para la obtención del factor de concentración de esfuerzos en el primer modo (modo  $I$ ) en un elemento mecánico durante la prueba de tensión, los campos de desplazamiento son obtenidos por Interferometría Electrónica del Moteado y la técnica de corrimiento de fase. Las deformaciones son calculadas mediante el método de diferenciación de Stokes. Los resultados obtenidos son comparados mediante una simulación usando el análisis de elemento finito.

**Descriptores:** Factor de intensidad de esfuerzo; interferometría electrónica de patrón de moteado; método de Stokes; corrimiento de fase.

PACS: 42.30.Ms; 02.60.Jh; 81.40.Jj; 81.40.Np

## 1. Introduction

T.J. Dolan [1] *et al.* state that all materials display defects in their internal structures that in one way or another modify their mechanical properties. This is the reason why it is complicated to obtain accurate results concerning the mechanical resistance of a material. The main theories that predict static failure are based on statistical analyses [2]. Two of these theories are the Von Mises-Hencky and Tresca's maximum shear stress theory, and are used as criterion of failure if material stresses over the yielding point [3]. However, many measurements under different stress conditions were observed with the aim to explain the fail process under a static load. Therefore, some degree of uncertainty is always present in the majority of such mathematical models; for example, Thomas J. Dolan *et al.* and Mischke, compared both the limit tensional fatigue and the flexing fatigue in independent works obtaining but not identical results [4]. In recent years, computer technical breakthroughs in finite element analysis (FEA) for the prediction of failure in mechanical elements have been developed [5]. The disadvantage of FEA techniques is that they are developed in a virtual environment, and often the structural model of one material is not exactly faithful to reality. For example, the stress intensity factor is obtained through a standard material with a well known elasticity modulus or stress-strain relationship, but inadequate constrains or boundary conditions which can be far for real ones causes wrong results. In the design and manufacturing processes, direct measurements are necessary to meet quality and safety standards [6]. Optical methods offer direct whole-field measurement of deformation processes. This is an advantage in comparison with other methods capable to measure deforma-

tions “in one-point” like strain gauges. However, digital image processing needs to be computed with special care because important data can be modify.

Electronic speckle pattern interferometry (ESPI), as a non-destructive technique, is capable of measuring directly whole-field displacements on the surface where the observation is made and stored in the computer memory [7,8]. Whole-field deformations are obtained from interferograms

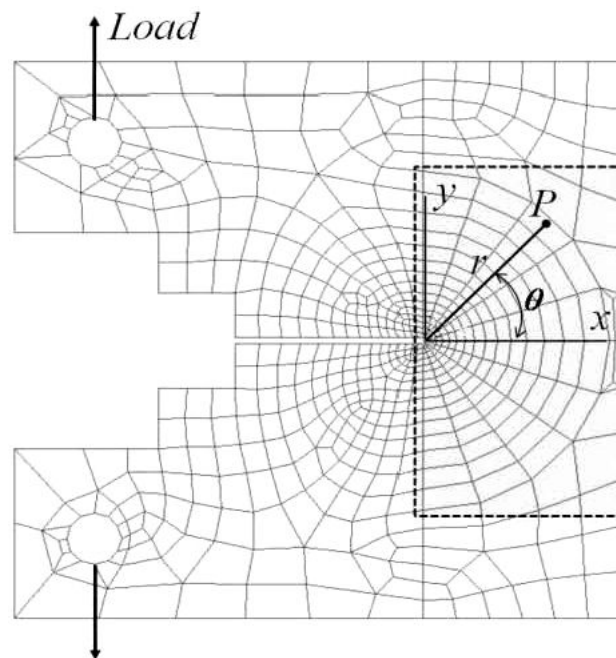


FIGURE 1. Test specimen geometry with a FEA mesh. The dotted line highlights the observation and analysis area.

in a computational post process means both any technique for interference phase extraction and the sensibility vector computation [9]. A high accuracy can be obtained with ESPI technique [10], however, the noisy characteristic of speckles induce errors when interferogram images are processed. Digital low band filtering needs to be applied to interferograms in aiming to reduce the speckle effect.

To measure the stress intensity factor (SIF) in mode *I* around a crack, we use a post-processing image analysis of the whole-field deformation images. Figure 1 shows the geometry of the test specimen used. The displacement whole-field is obtained through the electronic speckle pattern interferometry and phase stepping technique [11], and deformations are calculated by means of the Stokes differentiation method. In this paper, we present a comparison of results obtained through a finite element analysis technique and the measurements obtained by means of electronic speckle pattern interferometry.

## 2. Stress analysis for stress intensity factor estimation

Structural failure of mechanical elements can be a submissive state of stress, which always begins with a fracture in the

molecular structure of the material. These conditions lead to an excessive increase in the stress levels at the end of a crack [12]. However, since homogenous materials can display imperfections in their molecular structure, crack size and distribution depend on the manufacturing process and the quality of the material crafted. Furthermore, a simple scratch or a little superficial defect can be the beginning of a structural failure inasmuch as localized fractures and cracks create high levels of stress whose theoretical magnitude tends to infinity. No elastic material can be subjected to high levels of stress without experiencing local flow [13] and stress concentration around a crack. Another principle of stress concentration deals with the mechanical element's geometric shape [14]. Unsuitable geometric contours can modify stresses whole-field, while mechanical resistance is also modified by stress concentration; then, failure happens at load levels that are below what had originally been calculated. However, both the theory of linear-elastic mechanics of fractures and Hooke's law are totally applicable [15]. In this case, the mathematical model for displacements and the stress fields around a crack tip in Eqs. (1) and (2) are related to plane strain fields [16] through the Hooke's law in the elastic regimen and can be expressed as Eq. (3)

$$\begin{bmatrix} Iu(r, \theta) \\ Iv(r, \theta) \end{bmatrix} = \sum_{n=1}^{\infty} \frac{1}{2G} A_{In} r^{\frac{n}{2}} \begin{bmatrix} (3 - 4\mu) \cos\left(\frac{n\theta}{2}\right) - \frac{n}{2} \cos\left(\frac{n}{2} - 2\right)\theta + \left(\frac{n}{2} + (-1)^n\right) \cos\frac{n\theta}{2} \\ (3 - 4\mu) \sin\left(\frac{n\theta}{2}\right) + \frac{n}{2} \sin\left(\frac{n}{2} - 2\right)\theta - \left(\frac{n}{2} + (-1)^n\right) \sin\frac{n\theta}{2} \end{bmatrix} \quad (1)$$

$$\begin{bmatrix} \sigma_{xx}(r, \theta) \\ \sigma_{yy}(r, \theta) \\ \tau_{xy}(r, \theta) \end{bmatrix} = \sum_{n=1}^{\infty} \frac{n}{2} A_{In} r^{\frac{n-2}{2}} \begin{bmatrix} \left(2 + (-1)^n + \frac{n}{2}\right) \cos\left(\frac{n}{2} - 1\right)\theta - \left(\frac{n}{2} - 1\right) \cos\left(\frac{n}{2} - 3\right)\theta \\ \left(2 + (-1)^n + \frac{n}{2}\right) \cos\left(\frac{n}{2} - 1\right)\theta + \left(\frac{n}{2} - 1\right) \cos\left(\frac{n}{2} - 3\right)\theta \\ - \left((-1)^n + \frac{n}{2}\right) \sin\left(\frac{n}{2} - 1\right)\theta + \left(\frac{n}{2} - 1\right) \sin\left(\frac{n}{2} - 3\right)\theta \end{bmatrix} \quad (2)$$

$$\sigma_{xx} = E \frac{\partial Iu}{\partial x}, \quad \sigma_{yy} = E \frac{\partial Iv}{\partial y}, \quad \tau_{xy} = G \left( \frac{\partial Iu}{\partial y} + \frac{\partial Iv}{\partial x} \right). \quad (3)$$

The variables  $A_{In}$  are unknown coefficients related with the strain functions, when  $n = 1$  it is the stress intensity factor in mode *I*. The mathematical models of displacement are  $Iu(r, \theta)$  and  $Iv(r, \theta)$  in the *x* and *y* directions respectively.  $E$ ,  $G$  and  $\mu$  are elasticity constants: the Young's modulus, the shear modulus and the Poisson's ratio respectively. The coordinates  $(r, \theta)$  are polar coordinates with their origin at the crack ends. Equations (1) and (2) can be used for determining the stress intensity factor by a comparison of multiples measurements in the reference points coordinates of displacements obtained by ESPI and the displacement mathematical model. (See Fig. 2).

In order to find the unknowns coefficients  $A_{In}$  a linear equation system is obtained from Eqs. (1) or (2). To solve

the  $n$  number of unknowns, for example, using Eq. (1), an over-determinate data points near the crack tip is required with a least square procedure to minimize the error due to noisy data obtained from the speckle interferometry [17]. Let  $Su$  and  $Sv$  be defined by

$$Su = \sum_{k=1}^N (u_k(r, \theta) - Iu_k(r, \theta))^2 \quad (4)$$

$$Sv = \sum_{k=1}^N (v_k(r, \theta) - Iv_k(r, \theta))^2 \quad (5)$$

Where  $u, v$  are the  $k$  point data measurement by ESPI in the specimen test,  $N$  is the total of points data measurement

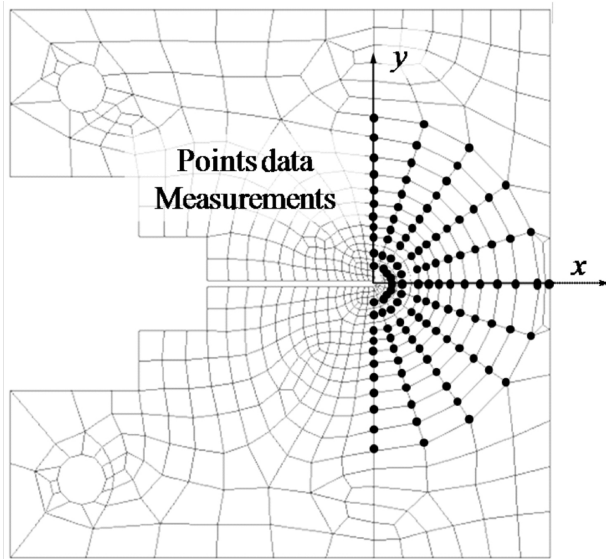


FIGURE 2. Reference data points used to obtain displacement measurements for SIF estimation.

and  $I_u, I_v$  are described in Eq. (1). Differentiating equations (4) and (5) with respect to  $A_{In}$  and equalizing to zero, we find a linear system of equations in terms of  $A_{In}$ . We can rewrite this in the form:

$$[S][A] = [C]. \tag{6}$$

Where the  $n \times 1$  matrices  $[C]$  and  $[A]$  are the constants and the unknowns related to the stress intensity factor respectively,  $[S]$  is a  $n \times n$  matrix of coefficients of  $A_{In}$ . The solution of Eq. (6) is given by:

$$[A] = [S]^{-1}[C]. \tag{7}$$

The stress intensity factor is determinate by the relationship [18]:

$$K_I = A_{I1}2\sqrt{2\pi} \tag{8}$$

On the other hand, theoretic results can be obtained by considering the specimen configuration. The theoretic stress intensity factor in mode  $I$  in the end of the crack tip is given by [19]:

$$K_I = \frac{F}{B\sqrt{W}}f\left(\frac{a}{W}\right), \tag{9}$$

where  $f(a/W)$  depends on the geometric and load configuration of the specimen test,  $B$  is the thickness,  $W$  the length and  $a$  is the crack length of the specimen.  $F$  is the applied load. A compact specimen as shown in Fig. 1 is defined as [19]:

$$f\left(\frac{a}{W}\right) = \frac{2 + \frac{a}{W}}{\left(1 - \frac{a}{W}\right)^{3/2}} \left[ 0.886 + 4.64\left(\frac{a}{W}\right) - 13.32\left(\frac{a}{W}\right)^2 + 14.72\left(\frac{a}{W}\right)^3 - 5.60\left(\frac{a}{W}\right)^4 \right] \tag{10}$$

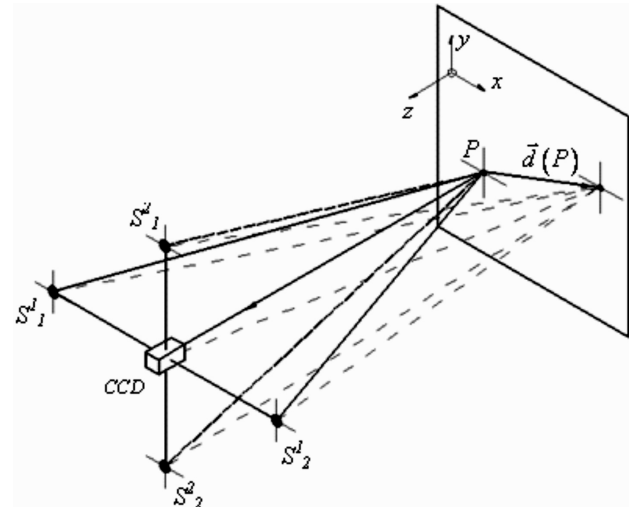


FIGURE 3. Schematic diagram of the optical setup for  $x$  and  $y$  in-plane sensitivity.

### 3. Optical setup

In a deformation process, each point  $P$  of the surface is displaced in its  $x, y$  and  $z$  coordinates. The displacement whole-fields on the surface can be represented by means of the displacement vector  $\vec{d}(P) = u(p) \cdot \hat{i} + v(p) \cdot \hat{j} + w(p) \cdot \hat{k}$ . To observe the displacement fields, an optical system with dual illumination is used to carry out a correlation of images before and after the undergoing of a deformation. Levels of image intensity  $I(x, y)$  of interferograms can be related to the deformations in the shape of fringes by means of the following equation:

$$I(x, y) = A(x, y) + B(x, y) \cos[\Delta\varphi(P)], \tag{11}$$

where interference phase  $\Delta\varphi(P)$  is related to the displacements on the surface,  $A(x, y)$  represents a constant term of intensity, and  $B(x, y)$  is a fringe modulation term of the interferogram. The displacement of  $P$  on the surface can be related to the phase by [20,21]:

$$\Delta\varphi(P) = \vec{e}(P) \cdot \vec{d}(P) \tag{12}$$

Sensitivity vector  $\vec{e}(P)$  depends both on the optical setup configuration and the wave length of the light sources. The deformed surface is simultaneously illuminated by two sources,  $S_1^i$  and  $S_2^i$ . The coordinates of the sources are  $(x_1^i, y_1^i, z_1^i)$  and  $(x_2^i, y_2^i, z_2^i)$  respectively;  $i = 1, 2$  depends of in-plane sensitivity direction,  $x$  or  $y$ . The optical setup is shown in Fig. 3.

Divergent illumination is used in our optical system. A. Martinez *et al.* [17], have demonstrated that one component of the in-plane sensitivity vector can be favored in some given

direction, while the sensitivity contribution in the orthogonal component is minimal. The component in direction  $z$  can be ignored since its sensitivity contribution is not greater than 0.1%. Then, Eq. (12) can be rewritten as a function of the displacement vector components  $\vec{d}(P)$  [22] by:

$$\begin{bmatrix} \Delta\varphi_x(P) \\ \Delta\varphi_y(P) \end{bmatrix} = \begin{bmatrix} e_x & 0 \\ 0 & e_y \end{bmatrix} \cdot \begin{bmatrix} u(P) \\ v(P) \end{bmatrix}. \quad (13)$$

Notice that the unitary deformation  $\varepsilon$  in their orthogonal components can be obtained by direct measurement of displacement fields  $u(P)$  and  $v(P)$  by:

$$\varepsilon_x = \frac{\partial u}{\partial x} \quad \text{and} \quad \varepsilon_y = \frac{\partial v}{\partial y} \quad (14)$$

To evaluate interference phase  $\Delta\phi$ , a relatively simple mathematical process is used. By adding  $n2\pi/N$  modulus displacement in the interference phase by means of a piezo-electric device, where  $N$  is the total number of steps, an image of each step ( $I_1, I_2, I_3, \dots, I_n$ ) is taken and archived in the computer memory,  $n=1,2,3, \dots, N$ . This technique is known as the phase stepping method. Equation (11) can be rewritten as:

$$I_n(x, y) = A(x, y) + B(x, y) \cos \left[ \Delta\varphi(P) + \frac{n2\pi}{N} \right] \quad (15)$$

Then, a linear system of three equations is created. For  $N = 3$ , and solving the linear system, a solution for the interference phase is [23]:

$$\Delta\varphi(x, y) = \arctan \left( \frac{\sqrt{3}(I_3(x, y) - I_2(x, y))}{2I_1(x, y) - I_2(x, y) - I_3(x, y)} \right). \quad (16)$$

The interference phases  $\Delta\varphi_x$  and  $\Delta\varphi_y$  are obtained from Eq. (16) switching illumination sources in the  $x$  and  $y$  direction of the optical setup respectively.

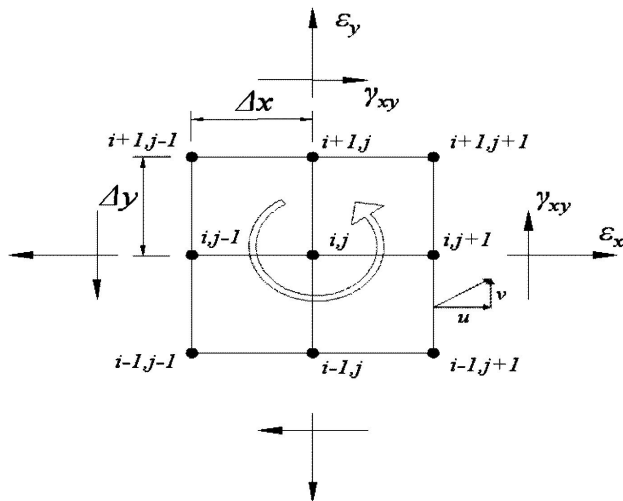


FIGURE 4.  $3 \times 3$  matrix used in the Stokes differentiation method around  $P(i, j)$ .

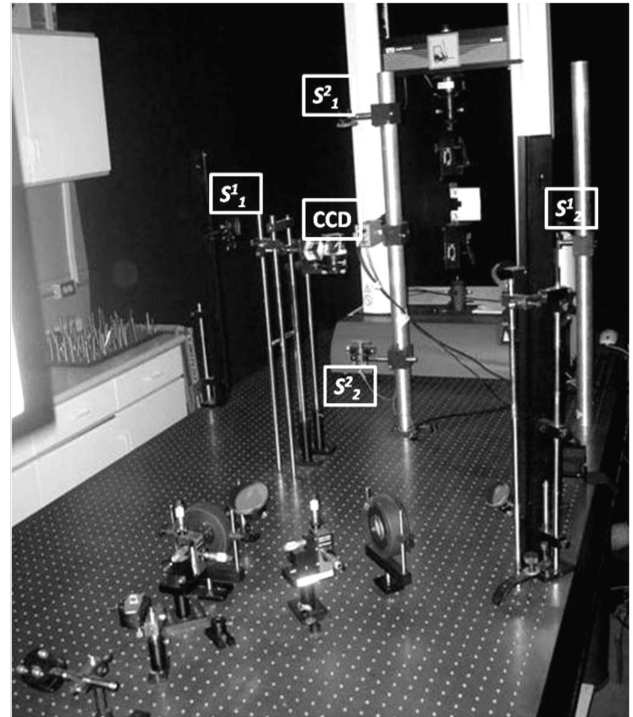


FIGURE 5. Experimental setup.

#### 4. Evaluation of strain by the Stokes method

In ESPI interferograms is common to obtain random noise due to the nature of the speckle phenomenon. It is known that the numerical differentiation of displacements whole-field produces unacceptable errors due to the computer calculations applied [24]. Some solutions to this problem involve the use of smooth interpolating functions, or the use of numerical methods to differentiate functions with low uncertainty. In this case, the derivatives are calculated by the Stokes method applied to a finite element of a surface in the plane  $x, y$ , as it is shown in Fig. 4, in such a way that  $dS = \Delta x \Delta y$ . Generally, we take  $\Delta x$  and  $\Delta y$  as the pixel-spatial resolution in the interferogram images; therefore, a matrix of  $3 \times 3$  pixels represents a surface of  $4\Delta x \Delta y$ . The displacement vector components  $u(P)$  and  $v(P)$  can be expressed by Stokes law at a point  $P(i, j)$  by [25]:

$$\oint_L \vec{d} \cdot \vec{dL} = \int_S (\nabla \times \vec{d}) \cdot \vec{dS} = \left( \frac{\partial v}{\partial x} - \frac{\partial u}{\partial y} \right) \cdot 4\Delta x \Delta y \quad (17)$$

Where the displacements and partial derivatives of  $w(P)$  are zero in the  $z$  direction. The term

$$\left( \frac{\partial v}{\partial x} - \frac{\partial u}{\partial y} \right) \cdot 4\Delta x \Delta y$$

represents the rotational displacement vector at a point  $P(i, j)$  of the surface within a closed line and it is related to the shearing strain  $\gamma_{xy}$  in this differential area. Then, using the trapezoidal rule for the standard integration of the

first term of Eq. (17), and eliminating orthogonal terms, we find [26]:

$$\oint_L \vec{d} \cdot d\vec{L} = [u_{i-1,j-1} + 2u_{i-1,j} + u_{i-1,j+1}] \cdot \frac{\Delta x}{2} - [u_{i+1,j+1} + 2u_{i+1,j} + u_{i+1,j-1}] \cdot \frac{\Delta x}{2} + [v_{i-1,j+1} + 2v_{i,j+1} + v_{i+1,j+1}] \cdot \frac{\Delta y}{2} - [v_{i+1,j-1} + 2v_{i,j-1} + v_{i-1,j-1}] \cdot \frac{\Delta y}{2} \quad (18)$$

The  $u$  and  $v$  terms are the weights of each pixel in a  $3 \times 3$  matrix. Notice that the scalar terms in Eqs. (17) and (18) can be used to find orthogonal components of strain by properly replacing the  $\Delta x$  and  $\Delta y$  terms. Using the previous equations, we obtain the following relationships:

$$\left(\frac{\partial u}{\partial y} + \frac{\partial v}{\partial x}\right) = [u_{i+1,j+1} + 2u_{i,j+1} + u_{i-1,j+1}] \cdot \frac{1}{8\Delta y} - [u_{i-1,j-1} + 2u_{i,j-1} + u_{i+1,j-1}] \cdot \frac{1}{8\Delta y} + [v_{i+1,j-1} + 2v_{i+1,j} + v_{i+1,j+1}] \cdot \frac{1}{8\Delta x} - [v_{i-1,j+1} + 2v_{i-1,j} + v_{i-1,j-1}] \cdot \frac{1}{8\Delta x} \quad (19)$$

$$\left(\frac{\partial u}{\partial x} + \frac{\partial v}{\partial y}\right) = [u_{i+1,j-1} + 2u_{i+1,j} + u_{i+1,j+1}] \cdot \frac{1}{8\Delta x} - [u_{i-1,j+1} + 2u_{i-1,j} + u_{i-1,j-1}] \cdot \frac{1}{8\Delta x} + [v_{i-1,j-1} + 2v_{i,j-1} + v_{i+1,j-1}] \cdot \frac{1}{8\Delta y} - [v_{i+1,j+1} + 2v_{i,j+1} + v_{i-1,j+1}] \cdot \frac{1}{8\Delta y} \quad (20)$$

### 5. Finite element analysis simulation

The finite element analysis in mechanical analysis is a numerical technique for finding approximate solutions of strain, stress and deformations. Many techniques to simulated stress-strain and deformations are reported, for example, A.A. Kotlyarenko *et al.* [23] present a simulation near a crack tip in a compact tensile specimen as shown in Fig. 1. Our model is based on eight-node finite element in two dimensions. This configuration of finite element provides more accurate results for mixed quadrilateral-triangular automatic meshes and can tolerate irregular shapes without as much loss of accuracy [27]. The 8-node elements have compatible displacement shapes and are well suited to model curved boundaries. The freedom degree of this is imitated in the  $u$  and  $v$  directions only. The numerical simulation was preformatted using the commercial software package ANSYS. Figures 7 and 8 show a comparison between ESPI and FEA simulation, they will be commented with more detail in the next chapter.

### 6. Experimental procedure and result analysis

A 6 mm thick test specimen was made out of aluminum 1050 A. Its mechanical properties were as follows: Young's modulus  $E = 71$  GPa, Poisson's ratio  $\mu = 0.334$ , and yield point  $S_{yp} 152$  MPa. The test specimen was mounted on an INSTRON<sup>®</sup> machine for tension tests (Fig. 5), an 8 bits CCD camera recorded images at 255 gray levels, the image dimensions were  $432 \times 326$  pixels, and the capture rate was 30 fps. The source of illumination was a He-Cd laser with a wavelength of 442 nm, located at coordinates (in millimeters):  $S_1^1 (-450,0,490)$ ,  $S_2^1 (452,0,490)$ ;  $S_1^2 (0,270,690)$ ,  $S_2^2 (0,-270,690)$ . Notice the increased sensitivity in the  $x$ -direction to compensate the deformation rate ( due to Poisson's ratio between  $u$  and  $v$ ). The maximum sensitivity vector component in the  $x$ -direction was  $19.7 \times 10^3$  rad/mm, while for the  $y$ -direction it was  $10.4 \times 10^3$  rad/mm.

The parameters of the universal machine were programmed at 0.125 mm/min; this is a minimum deformation speed between the ends of the test specimen. A preload of 0.5 kN was applied. Measurements were taken at every 20 N up to 2 kN. A low load was applied to avoid damage to the molecular structure of the test specimen. In order to verify the repetitive process, the relations of load-deformation for each test measurement were compared through the multiple measurements obtained. These data can be observed in Fig. 6. The processing time required for the phase stepping evaluation was almost 0.1 s, which represents a displacement in the observation area of about  $0.1 \mu\text{m}$  in the  $y$  direction. We can assume that the specimen deformation speed with respect to the speed of the image processing is sufficiently low to consider that the technique of phase stepping is executed in quasi-static conditions. Then, the rigid body translation that could be observed in interferograms is neglected. The image

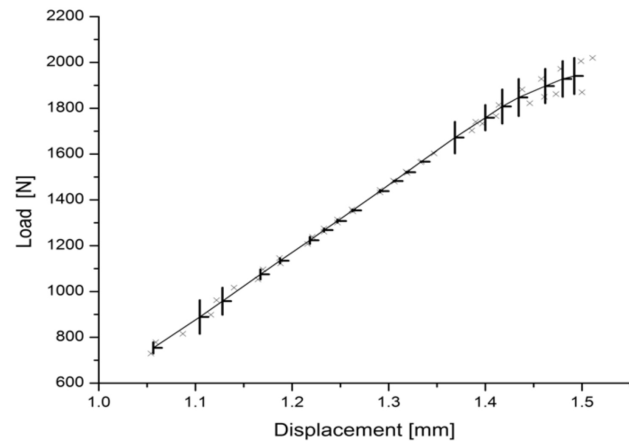


FIGURE 6. Relations of load-deformation obtained from multiple measurements.

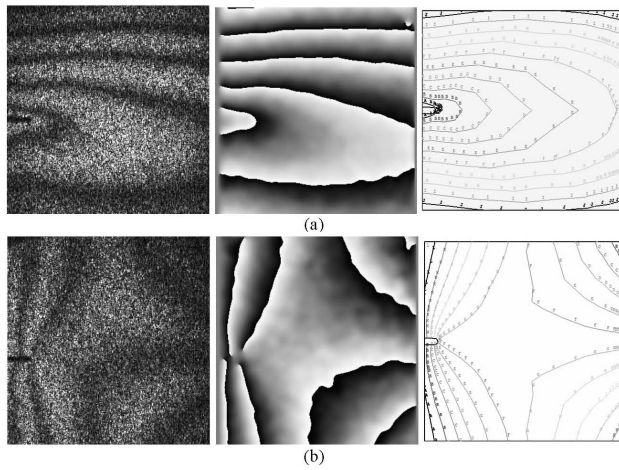


FIGURE 7. Fringe pattern, wrapped phase and FEA simulation to a)  $u$  displacements field, b)  $v$  displacement field; the applied load was 1.2 kN.

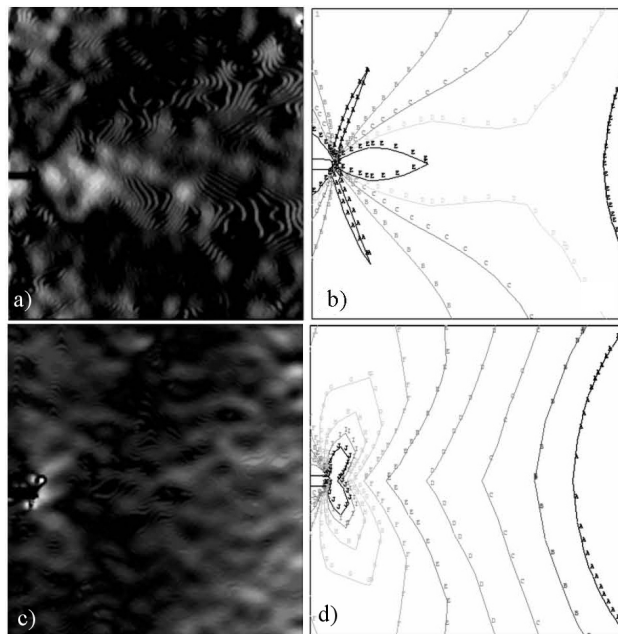


FIGURE 8. Strain whole-fields comparison obtained by ESPI after the Stokes method application and FEA simulation.  $\epsilon_x$  Deformation obtained by: a) ESPI, b) FEA;  $\epsilon_y$  deformation obtained by: c) ESPI, d) FEA; the applied load was 1.2 kN.

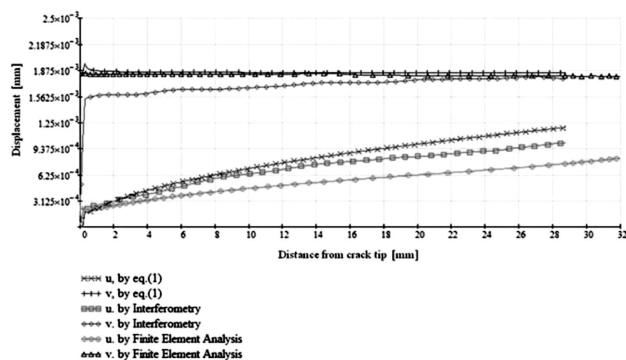


FIGURE 9. Displacements in the  $u$  and  $v$  directions at  $\theta = 0$ .

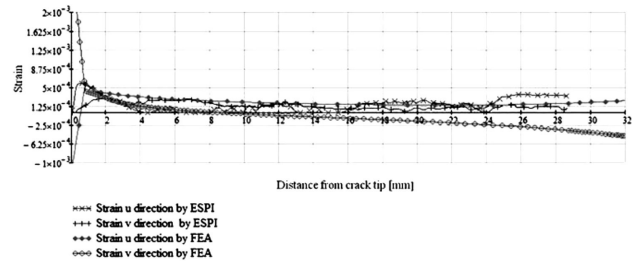


FIGURE 10. Strain obtained by ESPI and FEA techniques.

TABLE I. Stress intensity factor  $K_I$  obtained for the compact test specimen.

Applied Load (KN)	Stress Intensity factor $K_I$ (MPa $m^{0.5}$ )		
	Experimental ESPI	Numerical Eq. (6)	Finite element analysis
1.20	15.42	11.254	9.872
1.80	18.32	18.288	16.146

acquisition process was repeated at every load increment of 20 N, from the beginning until the end of the test. Each pair of illumination sources was switched during the test to obtain  $x$  and  $y$  sensitivity directions. The interferograms chosen for analysis were those that were between 1200 N and 1800 N.

Ignacio Lira *et al.* [21] refers to unacceptable errors in the direct application of numerical differentiation in noisy interferogram. Filtering of noisy data is necessary, but useful data are also to be inevitably lost in the edge of the specimen image. A convolution filtering process with a Gaussian kernel was applied on each interferogram like a low-pass frequency filter. The Gaussian kernel reduces considerably the noise with an acceptable lost of useful data in the specimen edge image. However, edge data's are not taken for SIF estimation. Then, a three step technique of phase stepping was used to get a whole-field phase associated with  $u$  and  $v$  displacement fields, (see Fig. 7). By using Stokes method, Eq. (20), we can find the strain whole-field. Figure 8 shows the results obtained for strain field.

We can see that  $u$  and  $v$  displacements measured with ESPI technique and strain whole-fields obtained through Stokes method agree with FEA analysis. However, we can see a little asymmetry in the  $u$  displacement of experimental fringes caused probably by a rigid rotation due to some alignment when a load was applied. In contrast, experimental fringes on the  $v$  displacement are symmetrical. Then, rigid body displacement can be dismissed. Figure 9 shows displacement results to FEA simulation, numerical computation and ESPI measurement along the  $x$  axis,  $\theta = 0^\circ$ . As we can see, displacements in the  $y$  directions is close to be a constant, but not in the  $x$  direction. This fact can be attributed to the constant movement of the tension test machine. The  $x$  displacements increase along  $\theta = 0^\circ$  due to the induced

momentum in the specimen. Figure 10 shows strain measurements along  $\theta = 0^\circ$  too. Near of the crack tip, FEA and ESPI strain measurements are similar. Table I shows results of the stress intensity factor  $K_I$  for loads of 1200 and 1800 N. Estimations of the maximum stress intensity factor gives 9.87 [MPa·mm<sup>0.5</sup>] to FEA at 1.2 kN and 18.32 [MPa·mm<sup>0.5</sup>] to ESPI measurement at 1.8 kN.

## 7. Conclusions

Electronic speckle pattern interferometry is a useful technique for strain analysis in machined elements. We can use both deformations and strain fields to compute the stress intensity factor. Complications can be associated with the presence of the speckle noise and the image resolution. The design of an appropriate low band pass filter is necessary to be applied to interferograms. However, important data can be affected, especially in the derivative process. The Stokes equations, usually associated to fluid mechanics, can be used for

a mechanical theory of elasticity if the deformation process is considered as a flow of very low velocity. Stokes method is an alternative method to get the derivative, since it takes at least eight elements around the analyzed data, in comparison to three or five data taken by traditional derivative methods. If the specimen deformation process is very slow, the phase stepping technique can be used with a tolerable error. Then, rigid body translation can be dismissed. Stress intensity factors obtained through FEA and ESPI techniques show similar results, once the speckle effect is reduced by a low band filtering. ESPI technique is useful to corroborate FEA predictions. Efficient mechanical design procedures can be attained using both techniques.

## Acknowledgements

Authors wish to thank economical support from Consejo Nacional de Ciencia y Tecnología (CONACYT).

1. T.J. Dolan, *SESA J. Exp. Mech.* **10** (1970) 1.
2. J. Marin, *Engineering Materials* (Prentice-Hall, Englewood Cliffs, N.J., 1952).
3. N.E. Dowling, *Mechanical Behavior of Materials* (Prentice Hall, Englewood Cliff, N.J., 1993).
4. J. Thomas Dolan, *Physical properties; ASME handbook-metals Engineering design* (McGraw-Hill, New York, 1953).
5. K. Ramesh and P.M. Pathank, *Commun. Numer. Methods Eng.* **15** (1999) 229.
6. M. Ravichandran, P.R.D. Karthick Babu, V. Rao, and K. Ramesh, *Strain* **43** (2007) 119.
7. L. Yang and A. Ettemeyer, *Opt. Eng.* **42** (2003) 1257.
8. D.B. Barker and M.E. Fourney, *Exp. Mech.* **17** (1977) 241.
9. A.J. Moore and J.R. Tyrer, *Opt. Lasers Eng.* **24** (1996) 381.
10. P.K. Rastogi, “*Digital Speckle Pattern Interferometry and Related Techniques*” (John Wiley & sons, Ltd. England, 2001).
11. K. Creath, *Appl. Opt.* **24** (1985) 3053.
12. L.P. Pook, *Linear Elastic Fracture Mechanics for Engineers, Theory and Applications* (WIT Press, Southampton, Boston, 2000)
13. N.E. Dowling, *Mechanical Behavior of Materials* (Prentice Hall, Englewood Cliff, N.J., 1993)
14. R.E. Peterson, *Stress concentration factors* (John Wiley & Son, New York, 1975).
15. F. Erdogan, *J. Appl. Mech.* **50** (1983) 992.
16. S.N. Atluri and A.S. Kobayashi, *Handbook on experimental mechanics*, 2nd ed. (ed. Kobayashi A.S.VCH SEM, New York, 1993)
17. W.J. Dally, C.A. Sciammarella, and J. Shareef, “*Determination of Stress Intensity Factor K from In-plane Displacement Measurements*” (Proc. of the Vth International Congress on Experimental Mechanics, Montreal 1984)
18. S. Yoneyama, T. Ogawa, and Y. Kobayashi, *Eng Fract Mech* **74** (2007) 1399.
19. T.L. Anderson, *Fracture mechanics, Fundamentals and applications* 2nd ed (CRC Press, Boca Raton, FL, 1991).
20. A. Martínez, J.A. Rayas, and R. Cordero, *Opt. Comm.* **262** (2006) 8.
21. H. Fan, J. Wang, and Y. Tan, *Opt. Lasers Eng.* **28** (1997) 249.
22. A. Martínez, J.A. Rayas, C. Meneses-Fabián, and M. Anguiano-Morales, *Opt. Comm.* **281** (2008) 4291.
23. T. Kreis, *Holographic Interferometry, principles and methods* (Akademie Verlag, Berlin, 1996).
24. I. Lira, R.R. Cordero, M. François, and C. Vial-Edwards, *Meas. Sci. Technol.* **15** (2004) 2381.
25. M. Raffel, C. Willert, and J. Kompenhans, *Particle Image Velocimetry: A Practical Guide* 1st ed, (Springer, Berlin, 1998); A.A. Kotlyarenko, T.A. Prach, V.V. Kharchenko, and A. Yu. Chirkov *Strength of Materials* **41** (2009) 106.
26. Rahman, I. Qazi, Schmeisser, and Gerhard, *Numerische Mathematik* **57** (1990) 123.
27. G. Villanueva, J.A. Plaza, E. González, and J. Bausells, *Microsyst Technol* **12** (2006) 455.